Desmosterol suppresses macrophage inflammasome activation and protects against vascular inflammation and atherosclerosis

Xinbo Zhang[a,b], Jeffrey G. McDonald[c,d], Binod Aryal[a,b], Alberto Canfrán-Duque[a,b], Emily L. Goldberg[b,e], Elisa Araldi[f], Wen Ding[a,b], Yuhua Fan[a,b], Bonne M. Thompson[c,d], Abhishek K. Singh[a,b], Qian Li[g], George Tellides[a,h], Jose Ordovás-Montanes[j,i], Rolando García Milian[k], Vishwa Deep Dixit[a,d], Elina Ikonen[l,m,1], Yajaira Suárez[a,n,b,1], and Carlos Fernández-Hernando[a,n,b,1]

[a]Vascular Biology and Therapeutics Program, Yale University School of Medicine, New Haven, CT 06520; [b]Integrative Cell Signaling and Neurobiology of Metabolism Program, Department of Comparative Medicine, Yale University School of Medicine, New Haven, CT 06520; [c]Center for Human Nutrition, University of Texas Southwestern Medical Center, Dallas, TX 75390; [d]Department of Immunobiology, Yale University School of Medicine, New Haven, CT 06520; [e]Department of Molecular Genetics, University of Texas Southwestern Medical Center, Dallas, TX 75390; [f]Energy Metabolism Laboratory, Institute of Translational Medicine, Department of Health Sciences and Technology, Swiss Federal Institute of Technology Zurich, Schwerzenbach CH-8603, Switzerland; [g]Department of Neuroscience and Kavli Institute for Neuroscience, Yale University School of Medicine, New Haven, CT 06520; [h]Department of Surgery, Yale University School of Medicine, New Haven, CT 06520; [i]Division of Gastroenterology, Boston Children's Hospital, Harvard Medical School, Boston, MA 02115; [j]Broad Institute of MIT and Harvard, Cambridge, MA 02115; [k]Bioinformatics Support Program, Yale University School of Medicine, New Haven, CT 06520; [l]Department of Anatomy, Faculty of Medicine, University of Helsinki, Helsinki 00014, Finland; [m]Minerva Foundation Institute for Medical Research, Helsinki 00290, Finland; and [n]Department of Pathology, Yale University School of Medicine, New Haven, CT 06520

Edited by Peter Tontonoz, University of California, Los Angeles, CA, and approved October 12, 2021 (received for review April 22, 2021)

Cholesterol biosynthetic intermediates, such as lanosterol and desmosterol, are emergent immune regulators of macrophages in response to inflammatory stimuli or lipid overloading, respectively. However, the participation of these sterols in regulating macrophage functions in the physiological context of atherosclerosis, an inflammatory disease driven by the accumulation of cholesterol-laden macrophages in the artery wall, has remained elusive. Here, we report that desmosterol, the most abundant cholesterol biosynthetic intermediate in human coronary artery lesions, plays an essential role during atherogenesis, serving as a key molecule integrating cholesterol homeostasis and immune responses in macrophages. Depletion of desmosterol in myeloid cells by overexpression of 3β-hydroxysterol Δ^{24}-reductase (DHCR24), the enzyme that catalyzes conversion of desmosterol to cholesterol, promotes the progression of atherosclerosis. Single-cell transcriptomics in isolated CD45$^+$CD11b$^+$ cells from atherosclerotic plaques demonstrate that depletion of desmosterol increases interferon responses and attenuates the expression of antiinflammatory macrophage markers. Lipidomic and transcriptomic analysis of in vivo macrophage foam cells demonstrate that desmosterol is a major endogenous liver X receptor (LXR) ligand involved in LXR/retinoid X receptor (RXR) activation and thus macrophage foam cell formation. Decreased desmosterol accumulation in mitochondria promotes macrophage mitochondrial reactive oxygen species production and NLR family pyrin domain containing 3 (NLRP3)–dependent inflammasome activation. Deficiency of NLRP3 or apoptosis-associated speck-like protein containing a CARD (ASC) rescues the increased inflammasome activity and atherogenesis observed in desmosterol-depleted macrophages. Altogether, these findings underscore the critical function of desmosterol in the atherosclerotic plaque to dampen inflammation by integrating with macrophage cholesterol metabolism and inflammatory activation and protecting from disease progression.

cholesterol | immunometabolism | atherosclerosis | macrophages

Atherosclerosis is the buildup of cholesterol-filled deposits called plaque within the inner layer of arteries as a consequence of the accumulation and modification of low-density lipoproteins (LDLs) that are taken up by macrophages leading to the formation of "foam cells" (1–3). Macrophages adapt their gene expression profile to coordinate a fast and precise immune response to provide protection against microbial infections and maintain normal tissue homeostasis (4–6). To this regard, down-regulation of cholesterol biosynthetic genes in classically activated macrophages is linked to regulation of inflammatory reactions elicited by macrophages and inflammasome suppression (7–9). This supports the idea that innate immune responses regulate cholesterol homeostasis and that this modulation is instrumental to proper macrophage function. Along these lines, it is now recognized that cholesterol biosynthetic intermediates and biologically active cholesterol metabolites such as desmosterol, lanosterol, and 25-hydroxycholesterol (25-HC) are emergent immune regulators of macrophages in response to lipid overloading and innate immune activation,

Significance

Previous work has shown that foamy macrophages accumulate desmosterol, a cholesterol biosynthetic intermediate. However, the participation of desmosterol in regulating the functions of cholesterol-laden macrophages in the physiological context of atherosclerosis has remained elusive. In this work, we selectively deplete desmosterol by overexpressing DHCR24, the enzyme that catalyzes the conversion of desmosterol into cholesterol, in myeloid cells and demonstrate that desmosterol content in atherosclerotic plaque macrophages controls their function and activation. Molecular analysis of macrophages isolated from lesions revealed that depletion of desmosterol increases the expression of interferon-regulated genes and genes associated with "classical" macrophage activation. Together, our work provides molecular insights into the intimate links between cholesterol metabolism and inflammatory responses of macrophages during atherogenesis.

Author contributions: X.Z., E.I., Y.S., and C.F.-H. designed research; X.Z., J.G.M., B.A., A.C.-D., E.L.G., E.A., W.D., Y.F., B.M.T., A.K.S., and C.F.-H. performed research; G.T., V.D.D., and E.I. contributed new reagents/analytic tools; X.Z., J.G.M., B.A., A.C.-D., E.L.G., E.A., W.D., Y.F., B.M.T., A.K.S., Q.L., J.O.-M., R.G.-M., V.D.D., E.I., Y.S., and C.F.-H. analyzed data; and X.Z., Y.S., and C.F.-H. wrote the paper.

The authors declare no competing interest.

This article is a PNAS Direct Submission.

[1]To whom correspondence may be addressed. Email: carlos.fernandez@yale.edu, yajaira.suarez@yale.edu, or elina.ikonen@helsinki.fi.

This article contains supporting information online at http://www.pnas.org/lookup/suppl/doi:10.1073/pnas.2107682118/-/DCSupplemental.

Published November 15, 2021.

respectively (7–10). Desmosterol, the last biosynthetic sterol intermediate of the Bloch pathway (Fig. 1*A*), has been reported to accumulate via negative feedback regulation of 3β-hydroxysterol Δ^{24}-reductase (DHCR24) in response to cholesterol loading in vivo and to mediate antiinflammatory responses in vitro. However, despite being the most prevalent sterol intermediate that accumulates in human atherosclerotic coronary artery plaques (Fig. 1 *B* and *C* and *SI Appendix*, Fig. S1), its specific role in regulating cholesterol homeostasis and inflammatory responses of macrophages during the progression of atherosclerosis has not been elucidated. Here, we show that desmosterol deficiency in macrophages using agenerated transgenic mouse model promotes vascular inflammation and atherosclerosis. Depletion of desmosterol in macrophages resulted in impaired liver X receptor (LXR) activation, lipid accumulation, mitochondrial metabolic alterations, and enhanced inflammasome activaition. Taken together, our study demonstrates that desmosterol contributes to macrophage inflammatory response in vivo, playing a critical role in the outcome of cardiovascular disease.

Results and Discussion

Desmosterol Depletion in Macrophages Promotes Vascular Inflammation and Atherogenesis. To investigate how desmosterol accumulation in macrophages affects cholesterol metabolism,

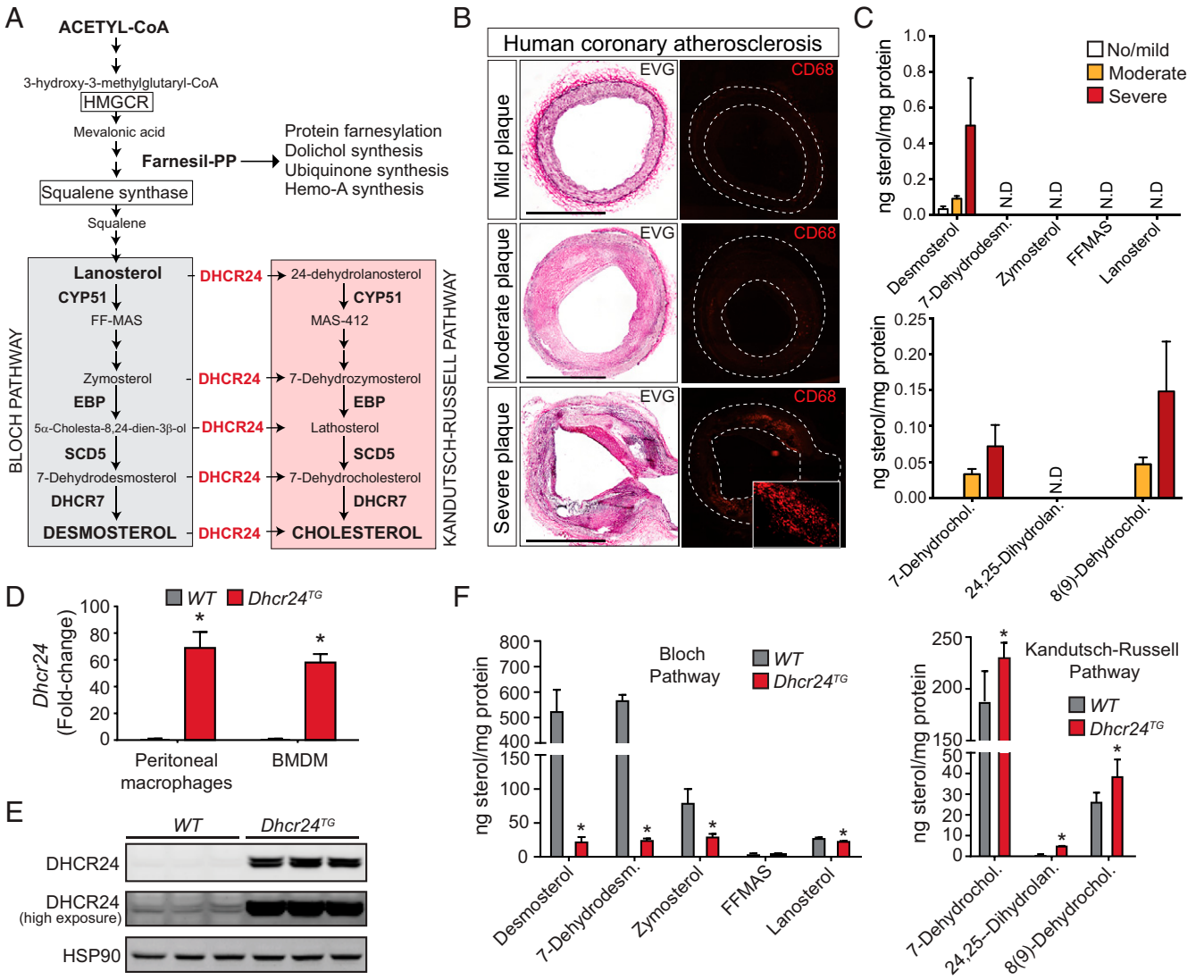

Fig. 1. Desmosterol is the most abundant cholesterol biosynthesis intermediate present in human coronary atherosclerotic plaque. (*A*) Schematic representation of cholesterol synthesis pathway. In the Bloch pathway, desmosterol is converted into cholesterol by DHCR24 in the final step. In the Kandutsch–Russell (K-R) pathway, lanosterol is converted into 24, 25-dihydrolanosterol by DHCR24 in the first step. DHCR24 might reduce the double bond in the side chain of the Bloch pathway sterols to generate sterols from K-R pathway. (*B*) Representative Verhoeff's Van Gieson (EVG) staining and immunofluorescence analysis of CD68 (macrophage marker) expression in atherosclerotic plaques isolated from human coronary arteries ($n = 4$ each group). (*C*) Lipidomic analysis of sterol biosynthetic intermediates in the Bloch (*Upper*) and K-R (*Bottom*) pathways in human coronary atherosclerotic plaques. Data were analyzed by one-way ANOVA, post hoc Dunnett's multiple comparison test ($n = 4$ per group). N.D. not detected. (*D*) qRT-PCR analysis of *Dhcr24* mRNA expression in peritoneal macrophages and BMDMs from WT and *Dhcr24*^{TG} mice. Data were analyzed by an unpaired two-sided Student's *t* test ($n = 3$ per group). (*E*) Representative Western blot analysis of DHCR24 expression in thioglycollate-elicited peritoneal macrophages from WT and *Dhcr24*^{TG} mice ($n = 3$ per group). (*F*) Quantification of sterol biosynthetic intermediates in the Bloch (*Left*) and K-R (*Right*) pathways in peritoneal macrophages isolated from WT ($n = 3$) and *Dhcr24*^{TG} ($n = 4$) mice. Data were analyzed by an unpaired two-sided Student's *t* test. Data represent the mean ± SEM; $^*P < 0.05$ compared to WT group. (Scale bar, 1 mm.)

inflammation, and atherosclerosis, we generated a conditional transgenic mouse that overexpresses DHCR24, the enzyme that converts desmosterol to cholesterol, in myeloid cells ($Dhcr24^{TG}$; *SI Appendix*, Fig. S2). Overexpression of *Dhcr24* in myeloid cells significantly increased *Dhcr24* messenger RNA(mRNA) (Fig. 1*D*) and protein (Fig. 1*E*) levels in both bone marrow–derived macrophages (BMDMs) and thioglycollate-elicited peritoneal macrophages. As a result, the content of desmosterol and upstream sterol intermediates was markedly reduced (up to 20-fold) in macrophages isolated from $Dhcr24^{TG}$ mice compared to wild-type (WT) mice (Fig. 1*F*). We next evaluated the effect of desmosterol depletion in macrophages during atherogenesis by injecting WT and $Dhcr24^{TG}$ mice with an adeno-associated virus encoding a gain of function form of PCSK9 (AAV8-*Pcsk9*) to induce hypercholesterolemia. We found no changes in body weight, plasma lipids, lipoprotein profiles, or circulating leukocytes (*SI Appendix*, Fig. S3). However, $Dhcr24^{TG}$ mice developed significantly larger lesions compared to WT mice (Fig. 2 *A* and *B*). Not only was the lesion area increased in the $Dhcr24^{TG}$ mice, but the necrotic core was also bigger (Fig. 2*A*), which correlated with increased apoptosis and decreased proliferation of macrophages in the lesions from the transgenic mice (*SI Appendix*, Fig. S4 *A* and *B*). As a consequence, plaque macrophages were significantly reduced in the lesions of $Dhcr24^{TG}$ mice compared to WT mice (*SI Appendix*, Fig. S4*C*). Reduction of macrophage desmosterol did not influence collagen composition or smooth muscle cell (SMC) numbers in atherosclerotic plaques (*SI Appendix*, Fig. S4*C*). Together, these data suggest that desmosterol content in macrophages controls the progression of atherosclerosis and plaque stability.

Desmosterol Regulates Macrophage LXR Signaling In Vivo. To gain insight into the functional role of desmosterol in macrophages, we generated foamy macrophages in vivo by isolating thioglycollate-elicited macrophages from WT and $Dhcr24^{TG}$ mice fed a high-fat, high-cholesterol western diet (WD) for 3 mo and analyzed the effects of desmosterol depletion on cholesterol metabolism and gene expression (Fig. 2*C*). Similar to previous findings (10), we found that foamy macrophages accumulated desmosterol (*SI Appendix*, Fig. S5*A*). DHCR24 overexpression significantly reduced their desmosterol content (Fig. 2*D* and *SI Appendix*, Fig. S5*B*), without affecting intracellular cholesterol levels in macrophages isolated from CD-fed mice (*SI Appendix*, Fig. S5*C*). Notably, cholesterol content in foamy macrophages was increased in $Dhcr24^{TG}$ macrophages compared to WT mice (*SI Appendix*, Fig. S5*C*). Levels of oxysterols including 25-hydroxycholesterol (25HC) were similar in the aortic lesions of WT or $Dhcr24^{TG}$ mice injected with AAV8-Pcsk9 and fed a WD for 12 wk, as well as in primary macrophages, nonfoamy or foamy, isolated from both groups of mice (*SI Appendix*, Fig. S6). Since the generation of 25HC is mediated by cholesterol 25-hydroxylase (CH25H), which expression is induced by immune activation, we analyzed whether DHCR24 overexpression influences 25HC production in response to TLR4 activation. We found that after lipopolysaccharide (LPS) stimulation, both intracellular and secreted 25HC levels were similar in WT and $Dhcr24^{TG}$ macrophages (*SI Appendix*, Fig. S7). Together, these data indicate that enhanced levels of DHCR24 do not alter oxysterols content in resting and activated macrophages and in the aortas from mice overexpressing DHCR24 in macrophages.

We next analyzed how demosterol content influences gene expression in primary macrophages. RNA sequencing (RNA-seq) revealed that desmosterol depletion in macrophages significantly reduced LXR/retinoid X receptor (RXR) activation and other pathways associated with the progression of atherosclerosis, including IL-10 signaling (Fig. 2*E*). We further confirmed these data by the decreased induction of LXR-responsive genes in foamy macrophages isolated from $Dhcr24^{TG}$ mice compared to WT mice fed either standard chow diet (CD) or WD (Fig. 2*F* and *SI Appendix*, Fig. S8). Furthermore, the expression of ATP Binding Cassette Transporters A1 and G1 (ABCA1 and ABCG1), two bona-fide LXR-regulated genes that mediate cellular cholesterol efflux (11, 12), were reduced in macrophages overexpressing DHCR24 (Fig. 2*G*). Accordingly, macrophages depleted of desmosterol showed a marked increase in neutral lipid accumulation and foam cell formation (Fig. 2 *H* and *I*). Similar findings were observed in thioglycollate-elicited macrophages isolated from WT and $Dhcr24^{TG}$ mice and loaded with cholesterol (*SI Appendix*, Fig. S9*A*). Notably, treatment of these macrophages with TO90, a synthetic LXR agonist, rescued the reduction in ABCA1 and ABCG1 expression observed in $Dhcr24^{TG}$ macrophages, suggesting again that desmosterol is an endogenous key regulator of LXR responses in macrophages (*SI Appendix*, Fig. S9*A*).

Recent reports have shown that foam cell formation attenuates inflammatory responses due to suppression of TLR4-responsive genes (10). To test whether endogenous synthesis of desmosterol suppresses Kdo2 lipid A (KLA; a TLR4-specific agonist)–induced inflammation, we treated WT and $Dhcr24^{TG}$ thioglycollate-elicited macrophages with KLA and measured the expression of *Cxcl9*, *Cxcl10*, *Il6*, *Tnf-α*, and *Il1-β* (*SI Appendix*, Fig. S9*B*). TLR4-induced inflammation was significantly enhanced in desmosterol-depleted macrophages, consistent with an antiinflammatory effect of desmosterol. This effect was abrogated when the cells were cultured in presence of T090, indicating that the activation of LXR by desmosterol inhibits TLR4 signaling (*SI Appendix*, Fig. S9*B*). Additionally, we found that overexpression of DHCR24 increased the expression of several proinflammatory mediators *Nos2*, *Cox2*, and *Csf1*, and attenuated the expression of certain genes (*Ym1*) associated with antiinflammatory responses (*SI Appendix*, Fig. S9*C*). Together, these results are consistent with the hypothesis that desmosterol has a physiological role as an LXR ligand in vivo modulating cholesterol metabolism and inflammatory responses of foamy macrophages.

The fact that atherosclerotic plaques from $Dhcr24^{TG}$ mice were characterized by marked necrosis and accumulation of apoptotic macrophages leads us to investigate whether desmosterol content in macrophages influences their susceptibility to endoplasmic reticulum (ER) stress–induced apoptosis or their capacity to clear apoptotic cells (ACs). Consistent with the known role of LXR in regulating both processes (13, 14), we found that macrophages isolated from $Dhcr24^{TG}$ mice were more susceptible to ER stress–induced apoptosis (*SI Appendix*, Fig. S10*A*) and showed a significant reduction in efferocytic capacity (*SI Appendix*, Fig. S10*B*).

Desmosterol Deficiency Promotes Macrophage Inflammatory Response in Vascular Lesions. We next investigated the relevance of desmosterol in regulating inflammatory responses of aortic myeloid cells. To this end, we isolated $CD45^{+}CD11b^{+}$ cells by flow sorting from enzyme-digested aortas of WT and $Dhcr24^{TG}$ mice and performed single-cell transcriptomics. To cluster the cells with similar gene expression, we performed dimensionality reduction and graph-based clustering (SEURAT; *Materials and Methods*) and detected six myeloid clusters and a contaminating SMC cluster (Fig. 3*A*). Cells from the non-SMC clusters expressed canonical myeloid cell, monocyte, and/or macrophage markers, including *Cd14* and *Cd68* (Fig. 3*B*). Notably, we found that the population of inflammatory macrophages (*cluster 2*) characterized by the expression of proinflammatory chemokines and cytokines (*Ccl2*, *Ccl4*, *Ccl5*, *Ccl10*, and *Cxcl10*) and the proatherogenic $F10^{+}$ (Ly6c2-high) monocytes (*cluster 0*) were increased in aortic lesions from $Dhcr24^{TG}$ mice compared to WT mice (Fig. 3 *C* and *D*). In contrast, the proportion of resting macrophages (*cluster 4*) was higher in atheroma from WT

PHYSIOLOGY

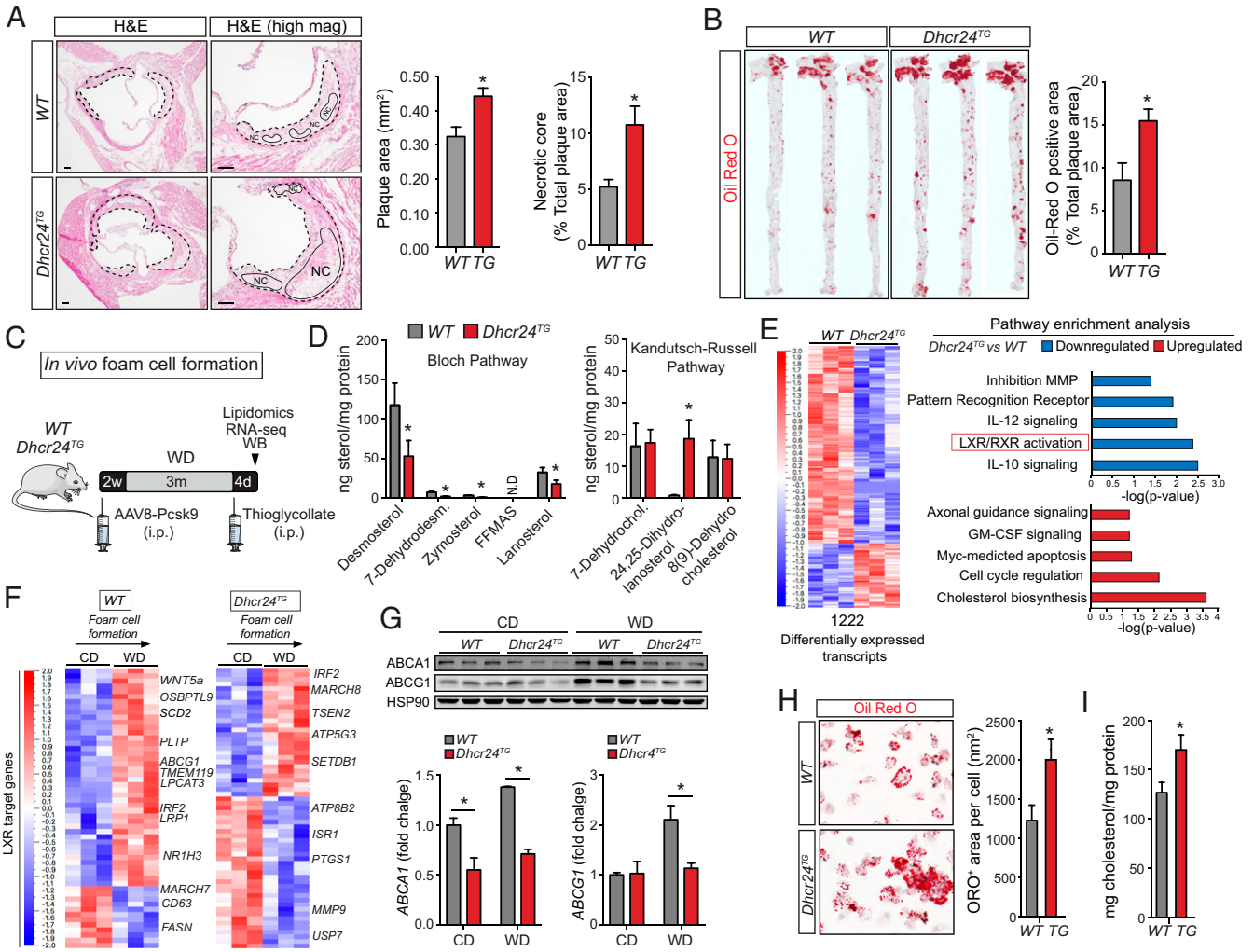

Fig. 2. Desmosterol depletion in myeloid cells promotes atherosclerosis. (*A*) Representative histological analysis of cross-sections of the aortic root stained with hematoxylin and eosin (H&E) of WT and *Dhcr24*^{TG} mice injected with AAV80-Pcsk9 and fed a WD for 16 wk. Dashed lines show the boundary of the developing necrotic core (NC). Quantification of plaque size and NC are shown on the *Right*. Data were analyzed by an unpaired two-sided Student's *t* test ($n = 10$ per group). (*B*) Representative en face ORO staining of aortas from WT and *Dhcr24*^{TG} mice injected with Pcsk9-Ad and fed a WD for 16 wk. Quantification of the ORO positive area is shown on the *Right* and represents the mean ± SEM ($n = 10$ per group). Groups were compared by an unpaired two-sided Student's *t* test. (*C*) Experimental protocol for isolation of in vivo macrophage foam cells. (*D*) Quantification of the Bloch and Kandutsch–Russell pathway sterols in macrophage foam cells isolated from WT and *Dhcr24*^{TG} mice injected with AAV8-Pcsk9 and fed a WD for 16 wk. Data were analyzed by an unpaired two-sided Student's *t* test ($n = 6$ per group), N.D., not detected. (*E*) Heat map depiction of all differentially expressed genes in foamy macrophages from WT mice compared to *Dhcr24*^{TG} mice. Pathway enrichment of differentially expressed genes expressed as the log[–P] analyzed by Ingenuity Pathway Analysis and is shown on the *Right*. (*F*) Heat map depiction of LXR target genes regulated in response to cholesterol accumulation (WD versus CD) in WT (*Left*) and *Dhcr24*^{TG} (*Right*) mice. Red shading indicates up-regulation and blue indicates down-regulation. (*G*) Representative Western blot analysis of ABCA1 and ABCG1 expression in macrophages isolated from WT and *Dhcr24*^{TG} mice injected with AAV8-Pcsk9 and fed a CD or WD diet for 16 wk. HSP90 was used as a loading control. Quantification is shown on the *Bottom*. Data were analyzed using two-way ANOVA with Bonferroni correction for multiple comparisons ($n = 3$ per group). (*H* and *I*) Representative ORO staining (*H*) and cellular cholesterol concentration (*I*) of peritoneal macrophages isolated from WT and *Dhcr24*^{TG} mice injected with AAV8-Pcsk9 and fed a WD diet for 16 wk. Data were analyzed by an unpaired two-sided Student's *t* test ($n = 6$ per group). Quantification represents the mean ± SEM; $^*P < 0.05$ compared to WT group. (Scale bar, 100 μm.)

mice (Fig. 3 *C* and *D*). The percentage of proliferating macrophages (*cluster 6*) was decreased in the transgenic mice, correlating with the reduced Ki67$^+$-CD68$^+$ cells observed in atherosclerotic plaques from *Dhcr24*^{TG} mice (*SI Appendix*, Fig. S4*B*). We also found a decreased trend in the proportion of lipid-associated macrophages (Cd63$^+$ cluster, Fig. 3*D*; *SI Appendix*, Fig. S11 *A*–*C*) in aortas isolated from *Dhcr24*^{TG} mice. However, we observed a significant increase of foamy macrophages in atherosclerotic aortas isolated from WT and *Dhcr24*^{TG} mice and analyzed by flow cytometry (*SI Appendix*, Fig. S11*D*) (15). We next analyzed the pathway enrichment analysis associated with changes in gene expression in CD45$^+$CD11b$^+$ cells. Among all the pathways that were significantly altered in response to the reduction of desmosterol in macrophages, we found the LXR/RXR pathway was significantly down-regulated in the *Dhcr24*^{TG} mice compared to WT mice, suggesting that desmosterol is the most relevant LXR ligand in atherosclerotic macrophages (Fig. 3*E*). Furthermore, interferon (IFN)-responsive genes were markedly increased in myeloid cells isolated from the transgenic mice (Fig. 3 *E* and *F*), consistent with impaired LXR activation in transgenic mice and the known inhibitory action of LXR on IFN signaling (16). We further validated these findings by immunostaining for NOS2, an IFN-induced molecule in mouse atherosclerotic plaques isolated

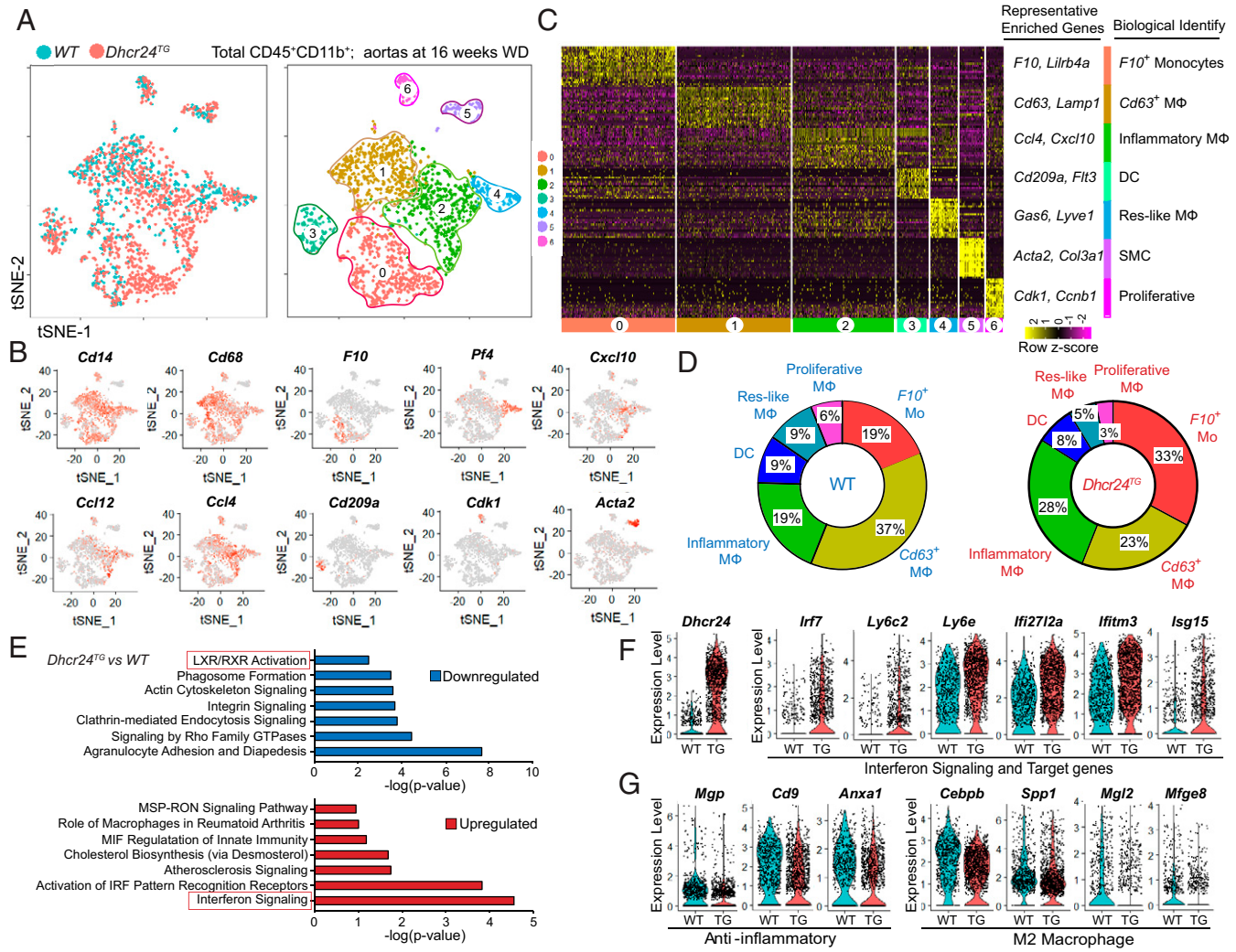

Fig. 3. Single-cell RNAseq analysis reveals increased interferon signaling in desmosterol-depleted myeloid cells isolated from mouse atherosclerotic lesions. (*A*) t-Stochastic neighbor embedding (t-SNE) representation of aligned gene expression data in single CD45^{+}CD11b^{+} cells extracted from atherosclerotic plaques of WT (n = 700) and *Dhcr24*^{TG} (n = 1,295) mice injected with AAV8-Pcsk9 and fed a WD for 16 wk. t-SNE dimensionality reduction analysis identified seven major clusters. (*B*) Feature plots depicting single-cell gene expression of individual genes. (*C*) Heatmap of the 20 most up-regulated genes in each cluster defined in *A* and selected as enriched genes used for biological identification of each cluster. (*D*) Proportions of defined cell populations extracted from the WT and *Dhcr24*^{TG} mice atherosclerotic aortas. (*E*) Pathway enrichment of differentially expressed genes as the log[–P] analyzed by Ingenuity Pathway Analysis. (*F* and *G*) Violin plots of the top differentially expressed genes showing statistically significant up-regulation (*F*) and down-regulation (*G*) in *Dhcr24*^{TG} CD45^{+}CD11b^{+} cells.

from *Dhcr24*^{TG} mice compared to WT mice (*SI Appendix*, Fig. S12). In addition to an increased interferon signature associated with classical macrophages, we also observed a marked suppression of antiinflammatory genes and tissue reparative markers in myeloid cells derived from *Dhcr24*^{TG} mice, indicating that desmosterol modulates macrophage activation toward a more resolutive and less inflammatory phenotype in atherosclerotic lesions (Fig. 3*G*). A potential limitation in the interpretation of these results is that the overexpression of DHCR24 also decreases lanosterol content in macrophages (Figs. 1*F* and 2*D* and *SI Appendix*, Fig. S5*B*), and lanosterol attenuates INF-β signaling and INF-β–stimulated gene expression (7), thus we cannot exclude that decreased levels of lanosterol observed in *Dhcr24*^{TG} macrophages might contribute to some extent to the increased of IFN-response genes observed in *Dhcr24*^{TG} compared to WT macrophages.

Macrophage Desmosterol Levels Regulate Inflammasome Activation. Previous work has suggested that the NLRP3 inflammasome is activated by cholesterol crystals in macrophages and that alteration in cellular cholesterol metabolism enhances mitochondrial reactive oxygen species (mtROS), leading to increased inflammasome activation (9, 17). Thus, we hypothesized that changes in desmosterol content in mitochondria might influence mitochondrial bioenergetics, which has been associated with macrophage inflammatory responses and inflammasome activation (18, 19). First, we immunopurified mitochondria from peritoneal macrophages isolated from WT and *Dhcr24*^{TG} mice. *Dhcr24*^{TG}-derived macrophage mitochondria had significantly reduced levels of desmosterol compared to macrophage mitochondria obtained from WT mice (*SI Appendix*, Fig. S13*A*). Interestingly, we found that decreased levels of desmosterol in mitochondria attenuated the respiratory capacity (*SI Appendix*, Fig. S13*B*) and increased glycolysis (*SI Appendix*, Fig. S13*C*) and mtROS production (*SI Appendix*, Fig. S13*D*), leading to increased inflammasome activation in *Dhcr24*^{TG} macrophages (Fig. 4*A*). This effect was independent of mitochondria number and morphology, which were similar in WT and *Dhcr24*^{TG} macrophages (*SI Appendix*, Fig. S14). In contrast to the enhanced inflammasome activation and *Il1-β*

levels observed in desmosterol-deficient macrophages, desmosterol loading, or DHCR24 inhibition using Triparanol (to promote desmosterol accumulation), significantly reduced *Il1-β* production, supporting that desmosterol content in macrophages influences inflammasome activation (*SI Appendix*, Fig. S15). We further determined whether desmosterol content influences inflammasome activation in vivo. To this end, we assessed neutrophilic peritonitis, a well-established model for inflammasome activation that measures neutrophil accumulation in the peritoneum in response to monosodium urate crystals (MSUs) (8). Similar to the results found in vitro, desmosterol depletion in macrophages resulted in markedly more MSU-induced neutrophil recruitment (Fig. 4*B*). Additionally, we found that *Il1-β* levels were also increased in atherosclerotic aortas from *Dhcr24*^{TG} mice compared to WT mice (Fig. 4 *C* and *D*). Together, these experiments identify desmosterol as a key molecule that controls macrophage inflammatory transcriptome profile and inflammasome activation in vitro and in vivo.

Genetic Ablation of *Nlrp3* and *Asc* Attenuates the Exacerbated Atherosclerosis Observed in *Dhcr24*^{TG} Mice. Next, we sought to explore the contribution of enhanced inflammasome activation observed in *Dhcr24*^{TG} mice during the progression of atherosclerosis. We generated WT and *Dhcr24*^{TG} mice lacking the inflammasome components NLRP3 or apoptosis-associated speck-like protein containing a CARD (ASC), an adaptor molecule that

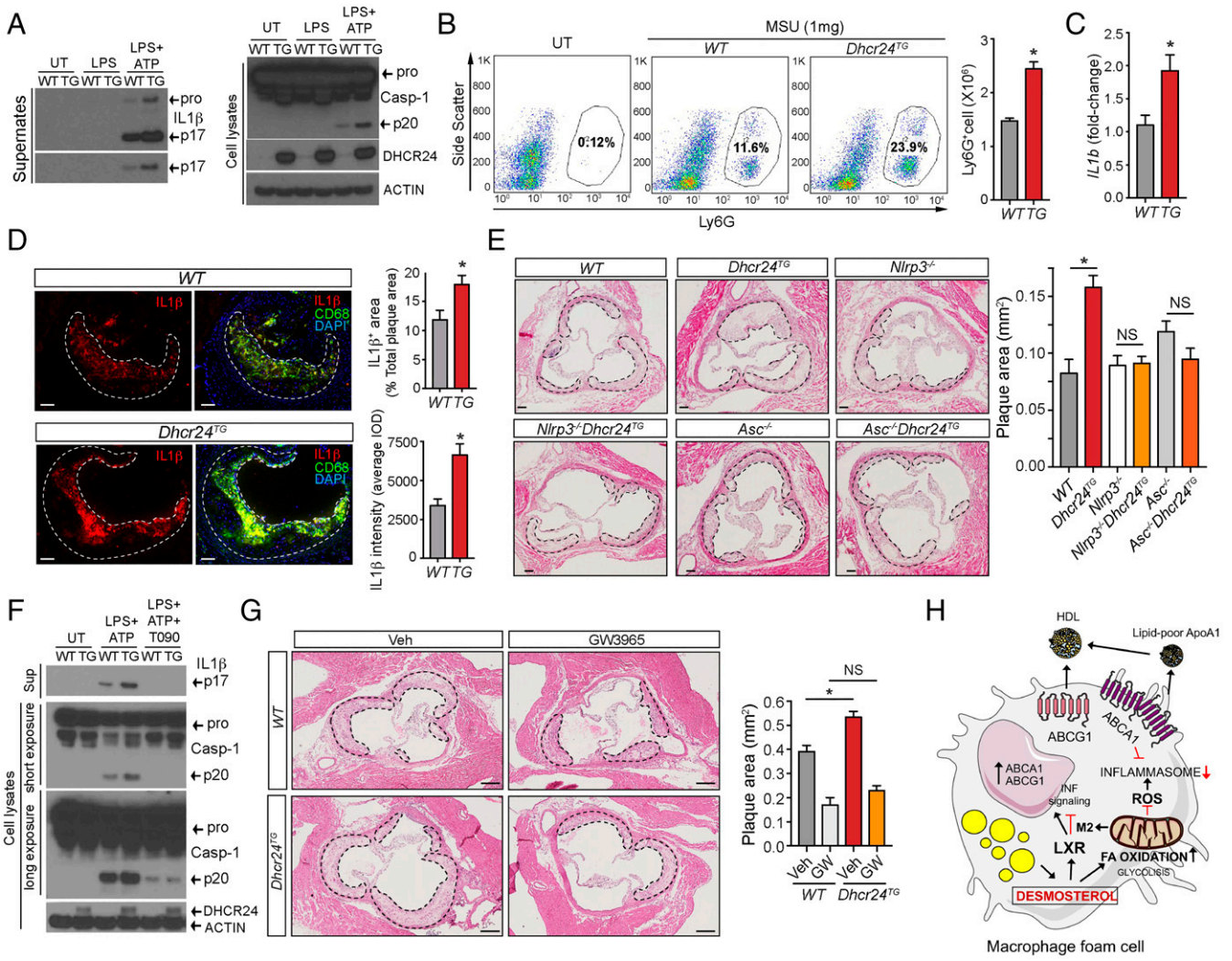

Fig. 4. NLRP3-dependent inflammasome activation is required for enhanced atherogenesis in *Dhcr24*^{TG} mice. (*A*) Representative Western blot analysis of IL-1β p17, Casp-1, DHCR24, and Actin expression in culture supernatants (*Left*) and cell lysates (*Right*) from untreated (UT) or LPS (1 μg/mL)–primed WT and *Dhcr24*^{TG} BMDMs after ATP (5 mM, 45 min) stimulation. (*B*) Representative FACS plots of peritoneal neutrophils (Ly6G^{+} cells) from mice injected intraperitoneally 6 h earlier with the MSU displaying percentage of Ly6G^{+} cells. Total number of peritoneal neutrophils from mice was quantified on the *Right*. Data were analyzed by an unpaired two-sided Student's *t* test ($n = 3$ per group). (*C*) qRT-PCR analysis of *Il1b* mRNA expression in atherosclerotic aortas from WT and *Dhcr24*^{TG} mice injected with AAV8-Pcsk9 and fed a WD for 16 wk. Data were analyzed by an unpaired two-sided Student's *t* test ($n = 3$ per group). (*D*) Representative immunofluorescence analysis of Il-1β and CD68 expression in atherosclerotic plaques from WT and *Dhcr24*^{TG} mice. Quantification is shown on the *Right*, and data were analyzed by an unpaired two-sided Student's *t* test ($n = 6$ per group). (*E*) Representative histological analysis of cross-sections of the aortic sinus stained with hematoxylin and eosin (H&E) from *Dhcr24*$^{fl/fl}$ (WT), *Dhcr24*$^{fl/fl}$*LysM*^{CRE} (*Dhcr24*^{TG}), *Nlrp3*$^{-/-}$, *Nlrp3*$^{-/-}$*Dhcr24*^{TG}, *Asc*$^{-/-}$, and *Asc*$^{-/-}$*Dhcr24*^{TG} mice injected with AAV8-Pcsk9 and fed a WD for 16 wk. Quantification of plaque size a is shown on the *Right* ($n = 5$ per group). Data represent the mean ± SEM; *$P < 0.05$ compared to WT group. (Scale bar, 100 μm.) (*F*) Representative Western blot analysis of IL-1β p17, Casp-1, DHCR24, and Actin expression in culture supernatants and cell lysates from UT or LPS (1 μg/mL)–primed WT and *Dhcr24*^{TG} BMDMs after ATP (5 mM, 45 min) stimulation in presence or not of T0901317 (T090). (*G*) Representative histological analysis of cross-sections of the aortic sinus stained with H&E of WT and *Dhcr24*^{TG} mice injected with AAV8-Pcsk9 and treated or not with GW3965. Quantification of plaque size a is shown on the *Right* ($n = 6$ to 8 per group). Data represent the mean ± SEM; *$P < 0.05$ compared to WT group. (Scale bar, 100 μm.)

interacts with NLPR3 to control inflammasome assembly. WT, $Dhcr24^{TG}$, $Nlrp3^{-/-}$-$Dhcr24^{fl/fl}$, $Nlrp3^{-/-}$-$Dhcr24^{fl/fl}$-$LysM^{CRE}$, $Asc^{-/-}$-$Dhcr24^{fl/fl}$, or $Asc^{-/-}$-$Dhcr24^{fl/fl}$-$LysM^{CRE}$ mice were injected with AAV8-Pcsk9 and fed a WD for 16 wk. Absence of *Nlrp3* or *Asc* either in WT and $Dhcr24^{TG}$ background did not influence plasma lipid levels or circulating blood cell counts (*SI Appendix*, Fig. S16 *A–C*). Notably, genetic deletion of either *Nlrp3* or *Asc* prevented the progression of atherosclerosis attributed to $Dhcr24^{TG}$ compared to WT mice (Fig. 4*E* and *SI Appendix*, Fig. S16*D*), suggesting that the increased atherosclerosis observed in mice overexpressing *Dhcr24* in macrophages is mediated by enhanced inflammasome activation. Surprisingly, we did not find any effect of *Nlrp3* or *Asc* deficiency on atherogenesis in $Ldlr^{-/-}$ mice. However, these results are in agreement with some studies showing that NLRP3 only contributed to the progression of atherosclerosis in the context of enhanced inflammasome activation caused by TET2 mutation or increased ROS production but not in $Ldlr^{-/-}$ mice (20–22). The elevated ROS production found in macrophages overexpressing DHCR24 supports this possibility.

Previous studies have shown that LXR activation might suppress inflammasome activation, while cholesterol accumulation and cholesterol crystal formation increase inflammasome activation (17, 22). Notably, we found that treatment of $Dhcr24^{TG}$ macrophages with a synthetic LXR ligand, TO90, attenuated the inflammasome activation observed in $Dhcr24^{TG}$ macrophages (Fig. 4*F*). Most importantly, the increased size in atherosclerotic lesions found in $Dhcr24^{TG}$ mice was markedly decreased in mice treated with GW3965 (LXR ligand) (Fig. 4*G*). However, we found that intracellular cholesterol levels were similar between WT or $Dhcr24^{TG}$ peritoneal macrophages stimulated or not with LPS (*SI Appendix*, Fig. S5 *C* and *D*). Furthermore, isolation of peritoneal macrophages from WT and $Dhcr24^{TG}$ mice was performed in CD-fed mice and used for inflammasome activation. These results suggest that increased inflammasome activation found in $Dhcr24^{TG}$ macrophages is not likely to a consequence of differences in cholesterol content, 25HC accumulation, or cholesterol crystal formation between WT and $Dhcr24^{TG}$ macrophages but to differences in LXR activation. Together, these results demonstrate that desmosterol is the key LXR ligand in vivo, and its absence impairs macrophage cholesterol efflux and promotes vascular inflammation and atherosclerosis (Fig. 4*H*).

The data gathered in atherosclerosis development in $Dhcr24^{TG}$ mice implies that desmosterol is essential for the progression of atherosclerosis in humans. To assess whether changes in expression in *DHCR24* in human aortas were causal for differences in atherosclerosis diagnosis, Mendelian randomization was used (23). This approach uses genetic data to measure causal relationships between genetically determined risk factors, which are phenotypic changes mediated by genetic variants, or instruments, assumed to be unbiased proxies and randomly distributed in the population, and measured outcomes, such as diagnosis or other health-related traits. In this case, the changes in *DHCR24* expression in aorta measured as expression quantitative trait loci (eQTLs) obtained from GTEX were used as exposure, or instrumental variables, while the risk of IC10 I70 diagnosis of atherosclerosis calculated in from genome-wide association study (GWAS) summary statistics, was the outcome. The model shows a significant causal estimate indicating that decreased expression of *DHCR24* might cause protection against atherosclerosis and vice versa (Fig. 5). Interestingly, the same single nucleotide polymorphisms (SNPs) with aorta eQTLs for DHCR24 show an inverse association with LDL blood GWAS summary statistics, suggesting that the cause of the protection from atherosclerosis diagnosis for downregulation of aortic DHCR24 is not the decrease in LDL (which is actually increased) (Fig. 5) but to other local factors and likely due to DHCR24-dependent accumulation of desmosterol in plaques.

Macrophage activation and differentiation prominently feature the modulation of genes involved in general cellular metabolic activities. Lipid metabolism is profoundly affected as one of the most conspicuous changes upon TLR4-mediated macrophage activation is eicosanoids production, while the downregulation of cholesterol biosynthetic genes in classically activated macrophages is linked to regulation of inflammatory reactions elicited by macrophages and inflammasome suppression (7, 24, 25). Cholesterol-loaded macrophages in atherosclerosis accumulate desmosterol as a consequence of a negative feedback regulation of DHCR24 expression. To better grasp the relevance of desmosterol in macrophage function during atherosclerosis, we opted to prevent its accumulation by overexpressing DHCR24. In this setting, we show that desmosterol is an endogenous mediator of both cholesterol efflux and antiinflammatory effects, functioning as the principal LXR activator of atherosclerosis-associated macrophages and a negative regulator of inflammasome activation. Additionally, DHCR24–induced alterations in macrophage sterol content content are linked to metabolic reprogramming toward aerobic glycolysis due to mitochondrial dysfunction (18, 19). The diminished desmosterol content in mitochondria attenuates the activities of the respiratory chain, allowing for ROS production and thus promoting the glycolytic metabolic switch, a hallmark of inflammatory macrophages. In addition to the direct effect of desmosterol in regulating mitochondrial bioenergetics, it could be possible that the activation of LXR by desmosterol might also mediate these effects. In this regard, it has been recently reported that LXR regulates the expression of Gramd1a, Gramd1b, and Gramd1c (also known as Aster-A, Aster-B, and Aster-C), which mediate the transport of cholesterol from the plasma membrane to ER and from the ER to mitochondria (26, 27). Notably, suppression of Aster-B impairs the transport of cholesterol from ER to mitochondria, leading to a significant reduction of cholesterol content and mitochondrial respiration (27). Altogether, our work provides insights into the intimate links between cholesterol metabolism and inflammatory responses of macrophages and prompts a reconsideration of existing therapies to develop of desmosterol-targeted interventions for modulating macrophage functions in atherosclerosis.

Materials and Methods

Generation of ROSA26-Dhcr24 Conditional Knock-In Mice. To investigate the specific role of desmosterol in macrophage functions and atherogenesis, we generated a conditional knock-in mouse by inserting a *Dhcr24* transgene expression cassette into the Rosa26 locus. The transgene is driven by the ubiquitous CAG promoter and is interrupted by a loxP-stop-loxP cassette to render *Dhcr24* expression inducible by the Cre recombinase followed by neomycin resistance gene flanked by FRT sites. The mice were mated with mice expressing FLP recombinase (JAX stock No. 009086) to excise the neomycin resistance gene to generate mice with DHCR24 conditional alleles ($Dhcr24^{fl/fl}$). Homozygous $Dhcr24^{fl/fl}$ mice were crossed with the transgenic mice expressing Cre recombinase under the control of the lysozyme 2 promoter/enhancer (JAX stock No. 004781). In the presence of Cre, recombination at the loxP sites excises the STOP cassette, thus activating expression of the DHCR24 specifically in the myeloid cell lineage. Offspring inheriting both the targeted allele and the Cre transgene ($Dhcr24^{fl/fl}$-$LysM^{CRE}$) were crossed with $Dhcr24^{fl/fl}$ mice to yield homozygous $Dhcr24^{fl/fl}$ littermates with (myeloid cell specific–DHCR24 knock-in or $Dhcr24^{TG}$) or without (WT, used as controls for experiments) Cre transgene. Agarose gel electrophoresis was performed to confirm the successful establishment of floxed mice, with or without the LysM-Cre transgene. PCSK9 adeno-associated virus (AAV8-Pcsk9) was injected intraperitoneally (1.0×10^{11} vector genome copies) to WT or $Dhcr24^{TG}$ mice (8 wk old, male) to promote the degradation of hepatic LDLR and increase circulating cholesterol levels (28). At 2 wk after injection, animals were fed either a standard CD or WD (40% fat and 1.25% cholesterol, ResearchDiets, D12108) for 16 wk to accelerate atherosclerosis. All the experiments were approved by the Institutional Animal Care Use Committee of Yale University School of Medicine.

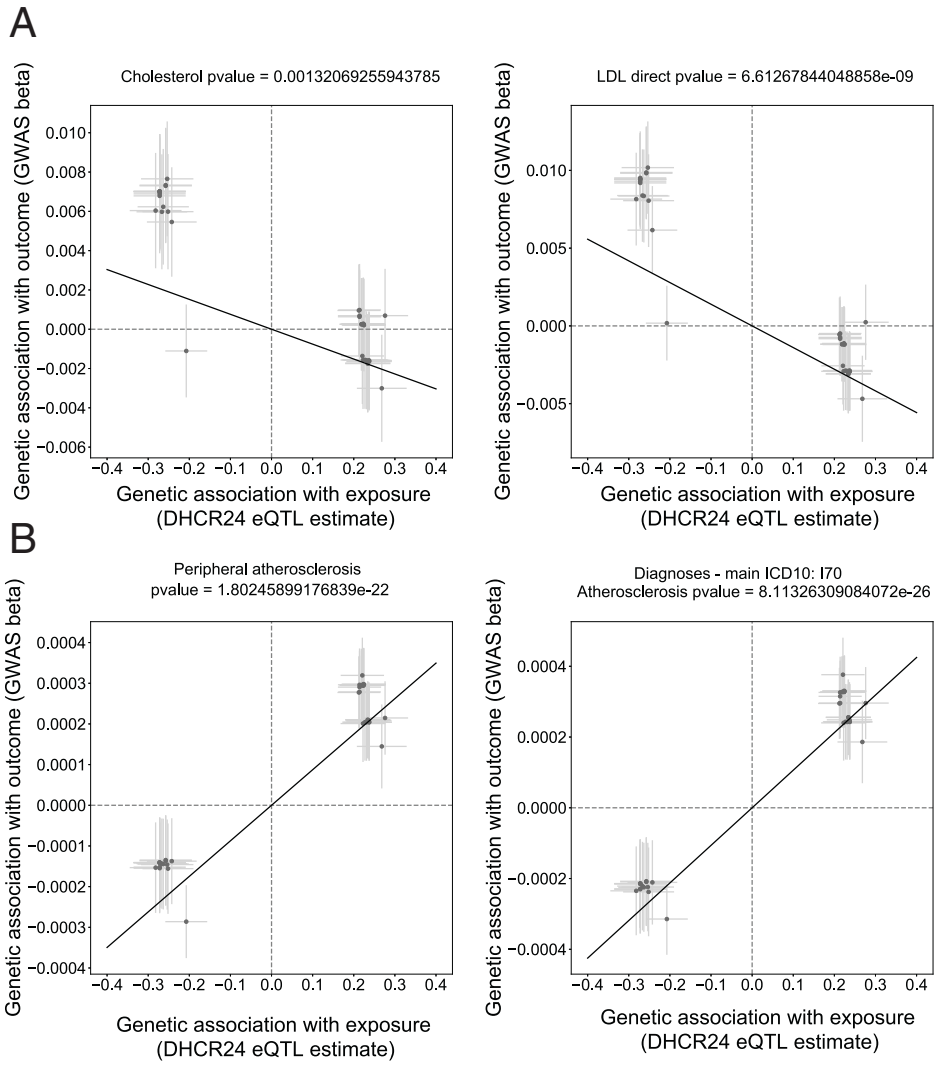

Fig. 5. Exposure–outcome plot of Mendelian randomization analysis of Dhcr24 expression in aorta (exposure) and cholesterol, LDL, or diagnosis of atherosclerosis (outcome). SNPs with significant aorta DHCR24 eQTLs were analyzed against their beta from GWAS on cholesterol, LDL, or diagnosis of atherosclerosis. Slope indicates Mendelian randomization estimate obtained with an inverse-variance weighted (IVW) model. Summary data were obtained from Neale laboratory public GWAS summary statistics and eQTL data from GTEx consortium.

Bone Marrow Transplantation Experiments. The *Dhcr24*^{TG} mice were crossed with NLRP3-deficient or ASC-deficient mice to obtain the *Nlrp3*$^{-/-}$-*Dhcr24*$^{fl/fl}$, *Nlrp3*$^{-/-}$-*Dhcr4*$^{fl/fl}$-*LysM*^{CRE}, *Asc*$^{-/-}$- *Dhcr24*$^{fl/fl}$, and *Asc*$^{-/-}$-*Dhcr24*$^{fl/fl}$-*LysM*^{CRE} mice. Bone marrow (BM) cells were obtained by flushing the tibias and femurs of age-matched (8-wk-old) mice. Transplantation was performed in *Ldlr*$^{-/-}$ mice lethally irradiated with 5 Gy twice in series and intravenously infused with 3×10^6 donor BM cells per recipient. At 5 wk after the transplantation, by which time the BM of the recipient mice was reconstituted, the mice were fed a WD diet for 16 wk to induce atherosclerosis.

Plasma Lipids and Lipoprotein Profile Analysis. Before and after WD feeding, mice were fasted for 12 to 14 h before blood samples were collected by retro-orbital venous plexus puncture. Plasma was separated by centrifugation and stored at −80 °C until analysis. Plasma total cholesterol (TC), high density lipoprotein-cholesterol (HDL-C), and triglyceride levels were determined by standard enzymatic methods (Wako Chemicals). Plasma cholesterol fractions (very low-density lipoprotein, intermediate-density lipoprotein/LDL, and HDL) were detected by fast-performance liquid chromatography gel filtration on Superose 6 HR 10/30 size-exclusion column (Pharmacia) as described previously (29).

Histology and Morphometric Analysis. Following anesthesia (100 mg/kg ketamine; 10 mg/kg xylazine), the thoracic cavity was exposed immediately, and in situ perfusion fixation through the left cardiac ventricle was performed by thorough perfusion with phosphate-buffered saline (PBS) and 4% paraformaldehyde (PFA). Subsequently, hearts and aortas were harvested and fixed in 4% PFA overnight. Hearts were embedded in optimal cutting temperature compound after dehydration with 30% sucrose and serial sections of aortic root were cut at 6-μm thickness using a cryostat. Every third slide from the serial sections was stained with hematoxylin and eosin for quantification of lesion area. Aortic lesion size of each animal was obtained by averaging the lesion areas in four sections from the same mouse. The necrotic core area was measured as a percentage of the total plaque area from three sections of the same mouse. Collagen content was assessed by Masson's Trichrome staining of consecutive slides from serial sections and quantified as a percentage of the total plaque area. For immunofluorescence imaging, CD68 (Serotec; No. MCA1957) and smooth muscle α-actin (α-SMA, Sigma; No. C6198) were used as macrophage and SMC markers, respectively, using consecutive slides from serial sections. Sections were incubated at 4 °C overnight with primary antibodies after blocking with blocker buffer (5% Donkey Serum, 0.5% bovine serum albumin [BSA], 0.3% Triton X-100 in PBS) for 1 h at room temperature (RT), followed by incubation with Alexa Fluor secondary antibody (Invitrogen) for 1 h at RT. The stained sections were captured using a Carl Zeiss scanning microscope Axiovert 200M imaging system, and images were digitized under constant exposure time, gain, and offset. Results are expressed as the percent of the total plaque area stained measured with the ImageJ software (ImageJ version 1.51, Yale software library, Yale University).

Blood Leukocyte Analysis. Blood was collected by retro-orbital puncture in heparinized microhematocrit capillary tubes. Erythrocytes were lysed with

ACK lysis buffer (155 mM ammonium chloride, 10 mM potassium bicarbonate, 0.01 mM ethylenediaminetetraacetic acid [EDTA], pH 7.4). White blood cells (WBCs) were resuspended in 3% FBS in PBS, blocked with 10 μg/mL FcgRII/III (Biolegend), then stained with a mixture of antibodies. Monocytes were identified as $CD115^{hi}$ and subsets as Ly6-C^{hi} and Ly6-C^{lo}; neutrophils were identified as $CD115^{lo}$Ly6-C^{hi}Ly6-G^{hi}. The following antibodies were used (BioLegend, 1:300 dilution): FITC-Ly6-C (AL-21), PE-CD115 (AFS98), and APC-Ly6-G (1A8). WBC and platelet counting in circulation was determined from EDTA-anticoagulated blood using a hemocytometer (Hemavet Counter HV950FS).

Aortic $CD45^{+}CD11b^{+}$ Cell Isolation from Atherosclerotic Lesions. To obtain the monocytes/macrophages in the atherosclerotic lesions, the aorta was digested (from the root to the diaphragm) with 1 mg/mL Collagenase A (Roche, Cat No. 11088785103) for 7 min at 37 °C to remove the adventitia under microscope. Aortic tissue was cut into small pieces and subjected to enzymatic digestion with 1.5 mg/mL Collagenase A and 0.5 mg/mL Elastase (Worthington, Cat No. LS006365) for 40 min at 37 °C while shaking. The digested aortas were passed through a 70-μm cell strainer to obtain single-cell suspensions followed by incubation of 10 min at 4 °C with 10 μg/mL of purified rat anti-mouse FcgRII/III (Biolegend) to block nonspecific binding of antibodies to Fc receptors. Total cell viability was obtained using live/dead viability dye eFluor 450 (Thermo Fisher Scientific). Cells were subsequently stained with rat-anti-mouse CD45-FITC (Biolegend, Cat No. 103108) and CD11b-APC (Biolegend, Cat No. 101212) at 4 °C for 30 min. Viable $CD45^{+}CD11b^{+}$ cells were sorted by a FACS Aria III (BD Biosciences) and immediately processed for single-cell RNAseq.

Droplet-Based Single-Cell RNA Sequencing (scRNA-seq) Library Construction and Sequencing. CD45 $^{+}CD11b^{+}$ cells were encapsulated into droplets and processed following manufacturer's specifications using 10X Genomics GemCode technology. Equal numbers of cells per sample were loaded on a 10x Genomics Chromium controller instrument to generate single-cell Gel Beads in emulsion (GEMs) at the Yale Center for Genome Analysis. Lysis and barcoded reverse transcription of polyadenylated mRNA from single cells were performed inside each GEM followed by complementary DNA (cDNA) generation using the Single-Cell 3′ Reagent Kits version 2 (10X Genomics). Libraries were sequenced on an Illumina HiSeq 4000 as 2 × 100 paired-end reads.

Single-Cell RNAseq Data Analysis. Sample demultiplexing, aligning reads to the mouse genome (mouse University of California, Santa Cruz mm10 reference genome) with Software Tools for Academics and Researchers (STAR) and unique molecular identifier (UMI) processing were processed using CellRanger software (version 2.1.1) as previously described (30). Low-quality cells, doublets, and potentially dead cells were filtered based on the percentage of mitochondrial genes and number of genes and UMIs expressed in each cell. After filtering, we identified 700 WT cells (a mean of 165,921 reads per cell, a median of 7,983 UMIs per cell, and a median 2,373 genes per cell) and 1,295 *DHCR24*^{TG} cells (a mean of 82,614 reads per cell, a median of 5,744 UMIs per cell, and a median 1,887 genes per cell) for downstream analysis. Data clustering was performed using Seurat R package (version 3.0) with filtered genes by barcode expression matrices as inputs (31). Highly variable genes (HVGs) were calculated using Seurat function *FindVariableGenes* and used for downstream clustering analysis. Principal component analysis (PCA) was performed with *RunPCA* function (Seurat) using HVGs for dimensionality reduction, and the number of significant principle components was calculated using *JackStraw* function. We applied the *RunTSNE* function to significant principal components (PCs) identified by *JackStraw* analysis and presented data in two-dimensional coordinates through t-distributed stochastic neighbor embedding generated by R package ggplot2. Clustering was done through *FindClusters* function using 27 significant PCs with a resolution of 0.4. Significantly differentially expressed genes in a cluster were analyzed using Seurat function *FindAllMarkers,* which were expressed in more than 25% of cells with at least 0.25-fold difference and reach statistical significance of an adjusted $P < 0.05$ as determined by the Wilcox test. Ingenuity Pathway Analysis (Ingenuity Systems QIAGEN, content version: 47547484, 2019) was used to carry out analyses for pathway with differentially expressed genes across samples.

En Face Oil-Red O Staining. A 35-mL Oil-Red O (ORO) stock solution (0.2% wt/vol in methanol) was mixed with 10 mL of 1 M NaOH and filtered. Aortas opened up longitudinally were briefly rinsed with 78% methanol, stained with 0.16% ORO solution for 50 min, and then destained in 78% methanol for 5 min (32). The stained sections were captured with an Olympus SZX16 stereo microscope and quantified with the ImageJ program. The lesion area was quantified as percent of ORO staining area in total aorta area.

Terminal Deoxynucleotidyl Transferase End Labeling. ACs in lesions were labeled by terminal deoxynucleotidyl transferase end labeling (TUNEL) using the in situ cell death detection kit TMR-red (Roche Diagnostics) according to the manufacturer's protocol. Briefly, frozen sections were fixed with 4% PFA and incubated with permeabilization solution (0.1% Triton X-100, 0.1% sodium citrate in PBS buffer) for 2 min on ice. After dialyzing extensively against PBS buffer for 30 min at RT, the slides were incubated with 50 μL TUNEL reaction mixture covered with parafilm pieces for 60 min at 37 °C in a humidified atmosphere in the dark. To identify specific cell types undergoing apoptosis, double staining was performed by combining TUNEL and immunohistochemistry for CD68 (macrophage marker). TUNEL staining sections were then viewed using inverted fluorescent microscope and photographed. Only TUNEL-positive cells that colocalized with DAPI-stained nuclei were counted as positive, and three sections of each mouse were quantified to detect the AC number.

Real-Time RT-PCR. Total RNA from thioglycollate-elicited peritoneal macrophages, BMDMs, or atherosclerotic aortas of WT or *Dhcr24*^{TG} mice was extracted using RNeasy mini kits (Qiagen) and reverse-transcribed into cDNA with iscript cDNA systhesis kit (Bio-Rad). Real-time PCR was conducted with gene expression levels with oligonucleotides specific for each of the genes. qPCR was performed with SsoFast EvaGreen Supermix (Bio-Rad) using the same thermal profile conditions for all primers sets: 40 amplification cycles (95 °C for 5 s and 60 °C for 10 s). All samples were analyzed in triplicate, and GAPDH content was used for normalization.

Western Blot. Cells were lysed in ice-cold radioimmunoprecipitation assay buffer (50 mM Tris·HCl, pH 7.4, 150 mM NaCL, 1% Nonidet P-40, 0.5% sodium deoxycholate, 0.1% sodium dodecyl sulfate [SDS]) supplemented with protease and phosphatase inhibitors (Roche Molecular Biochemicals). Cell lysates were rotated at 4 °C for 1 h before the insoluble material was removed by centrifugation at 12,000 × *g* for 10 min. After normalizing for equal protein concentration, cell lysates were resuspended in SDS sample buffer before separation by SDS-polyacrylamide gel electrophoresis and transferred onto 0.45-μm nitrocellulose membranes (Bio-Rad). Blots were then probed separately with primary antibodies: anti-DHCR24 (Cell Signaling, No. 2033), anti-ABCA1 (Abcam, ab18180), anti-ABCG1 (Novus Biologicals, NB400-132), anti-HSP90 (BD Biosciences, No. 610419), anti-IL1β (Genetex, GTX74034), anti-Caspase 1 (Genentech, 4B4.2.1), anti–β-actin (Cell Signaling, 4967L), anti-TOM20 (ABclonal, A6774), and anti-Calnexin (Cell Signaling, No. 2679). Following incubation with Alexa Fluor 680 (Invitrogen) and/or IRDye 800 conjugated AP (Rockland) secondary antibodies, images were collected using the Odyssey Infrared Imaging System (LI-COR Biotechnology). Densitometry analysis of the gels was carried out using ImageJ software from the NIH.

Foam Cell Formation In Vivo. WT-Pcsk9-Ad and *Dhcr24*^{TG}–Pcsk9-Ad mice were injected intraperitoneally with 3% thioglycollate broth to elicit peritoneal macrophages after 16 wk on CD or WD diet. Thioglycollate-elicited macrophages were allowed to attach on a coverglass for 30 min and then fixed by 4% PFA in PBS for 1 h. Cells were stained for 30 min with 0.3% ORO solution in 60% isopropanol. The mean area and integrated optical density of ORO-stained region per cell were quantified with 200 representative cells using ImageJ software from the NIH.

Cellular Cholesterol Analysis. To confirm the results of in vivo macrophage foam cell formation stained with ORO, the cellular TC level was detected with the Amplex Red Cholesterol Assay Kit (Thermo Fisher Scientific). Briefly, peritoneal macrophages were washed twice with PBS and centrifuged for 5 min at 300 × *g* for protein concentration assay and lipid extraction. The cell pellet was extracted with 200 μL chloroform: isopropanol: Nonidet P-40 (7:11:0.1) and centrifuged for 10 min at 15,000 × *g*. The liquid was then transferred to a new glass tube, and the organic solution was removed under vacuum. The dried pellet was reconstituted with cholesterol assay buffer from the kit, and the level of TC was detected following the kit manual. The results were expressed as cholesterol (μg) per total cell protein (mg).

M1/M2 Polarization and Inflammation Assay. BMDMs from WT or *Dhcr24*^{TG} mice were cultured in medium containing RPMI 1640 (Invitrogen) with 100 U penicillin/streptomycin and 10% lipoprotein-deficient serum (LPDS) for 48 h. For M1/M2 polarization analysis, cells were stimulated for 8 h with IL-4 (15 ng/mL, R&D, Cat No. 404-ML-010) and LPS (10 ng/mL, Sigma, L2630) plus IFN-γ (20 ng/mL, R&D, Cat No. 485-MI-100) to polarize macrophages to M2 or M1, respectively. For KLA Avanti Polar Lipids, Cat No. 699500)–induced inflammatory response, macrophages were pretreated with vehicle or the LXR-specific agonist T0901317 (3 μM, Cayman Chemical, Cat No. 71810) for 24 h, then treated with the TLR4-specific agonist KLA (100 ng/mL) for 6 h before harvesting for experiment as indicated. At the end of the treatments, cells

were extensively washed with 1× PBS, and RNA was isolated for macrophage polarization and inflammation analysis.

NLRP3 Inflammasome Activation. For inflammasome activation assays, BMDMs were plated at 10^6 cells/mL in RPMI 1640 containing 10% LPDS. Cells were primed with LPS (1 μg/mL, 4 h) followed by treatment with NLRP3 activator ATP (5 mM, Sigma-Aldrich, A7699) for 45 min. The cell supernatants and cell lysates were collected after ATP treatment and analyzed for caspase-1 (Genentech, 4B4.2.1) and IL-1β (Genetex, GTX74034) by Western blot. The cell supernatants was concentrated using Amicon Ultra 10K filtration units (Millipore), and the level of TNF-α was quantified by enzyme-linked immunosorbent assay (Biolegend).

Efferocytosis Assay. Peritoneal macrophages were recovered from mice as described in *Foam Cell Formation In Vivo*. A total of 5×10^5 cells were plated on sterile glass coverslips with RPMI 1640 (Invitrogen), 10% fetal bovine serum, and 20% L-cell–conditioned medium for 2 d. To generate ACs, Jurkat T cells were labeled with CellTracker Red (ThermoFisher, C34552) according to the manufacturer's instructions. Labeled cells were ultraviolet irradiated for 6 min using an 8-W bulb and incubated at 37 °C for 2 h to induce apoptosis. Fluorescent ACs were added to peritoneal macrophages in a 1:1 ratio (ACs:macrophages) and cultured at 37 °C for 60 min in RPMI 1640 supplemented with 10% FBS. After incubation with ACs, macrophages were gently washed several times with cold PBS with EDTA (0.6 μM) to remove free ACs. Cells were then fixed with 4% PFA, and the engulfment was scored with a Zeiss Axiovert 2000 M fluorescence microscope (Carl Zeiss). Efferocytosis was expressed as phagocytic index: number of cells ingested per total number of macrophages × 100. Macrophages were visualized with CD68 antibody (Serotec; No. MCA1957).

Collection of Human Specimens. Coronary arteries were collected from recipient hearts at the time of transplant explantation or donor hearts not used for clinical transplantation at the time of organ procurement. Coronary artery disease was categorized as none/mild, moderate, or severe based on inspection by an experienced cardiac surgeon. The right coronary artery was dissected from ostium to crux and placed in ice-cold saline for immediate transportation. Segments were divided in the laboratory and stored at −80 °C for sterol biosynthesis as described in *Preparation of Samples for Lipidomics* and *LC-MS/MS Analysis* or embedded in optimal cutting temperature medium at −80 °C for histology. Research protocols were approved by the Institutional Review Boards of Yale University and the New England Organ Bank. A waiver for consent was approved for surgical patients, and written informed consent was obtained from a member of the family for deceased organ donors.

Preparation of Samples for Lipidomics. Sterol biosynthesis in thioglycollate-elicited peritoneal macrophages and whole atherosclerotic aortas were analyzed by liquid chromatography with tandem mass spectrometry (LC-MS/MS) as described previously (33). Peritoneal macrophages were isolated from AAV8-Pcsk9–injected WT or *Dhcr24*^{TG} mice after 16 wk on a CD or WD diet and allowed to attach for 30 min. Cells were washed with PBS twice and then harvested in 1 mL Dulbecco's PBS. A 200-μl aliquot each cell lysate was reserved for measurement of protein concentration by a DC protein assay kit (Bio-Rad, Cat No. 5000111). The remaining cell lysate was centrifuged and the cell pellet was snap frozen in liquid N_2 and stored at −80 °C. Whole aortas from WT or *Dhcr24*^{TG} mice injected with AAV8-Pcsk9 were harvested 16 wk after WD feeding following thorough perfusion with PBS and snap frozen in liquid nitrogen and stored at −80 °C.

LC-MS/MS Analysis. Lipids were extracted from the samples by a modified Bligh–Dyer extraction, and sterols were analyzed by LC-MS/MS as described previously (33–35). Briefly, lipid extracts from samples were dried under nitrogen and reconstituted in 90% methanol. Sterols were analyzed using a Shimadzu LC20ADxr high-performance liquid chromatograph equipped with an Agilent Poroshell 120 EC-C18 column (2.1 × 150 mm, 2.7-μm particles; Agilent Technologies). The elution was done using a solvent gradient that transitioned linearly from 93% methanol/7% H_2O to 100% methanol in 7 min. The column was washed for 5 min in 100% methanol and then returned to the initial solvent. Sterols were detected using a SCIEX API 5000 triple quadrupole mass spectrometer equipped with a Turbo V APCI source in positive mode with atmospheric pressure chemical ionization at a temperature of 350 °C. Data were acquired under multiple reaction monitoring for mass pairs optimized for each sterol. The internal standards were commercially available for all but four of the sterols (dihydro-ff-MAS, dihydro-t-MAS, dehydrolathosterol, and dehydrodesmosterol) in the cholesterol biosynthetic pathway that were identified by their unique m/z values and retention times as described (33, 35).

RNAseq Analysis. Thioglycollate-elicited peritoneal macrophages were isolated from AAV8-Pcsk9–injected WT or *DHCR24*^{TG} mice after 16 wk on CD or WD diet. Total RNA was extracted and purified using a RNA isolation Kit (Qiagen) followed by DNase treatment to remove genomic contamination using RNA MinElute Cleanup (Qiagen). The purity and integrity of total RNA sample was verified using the Agilent Bioanalyzer (Agilent Technologies). Ribosomal RNA (rRNA) was depleted from RNA samples using Ribo-Zero rRNA Removal Kit (Illumina). RNA libraries from WT BMDMs were performed TrueSeq Small RNA Library preparation (Illumina) and were sequenced for 45 cycles on Illumina HiSeq 2000 platform (1 × 75-bp read length). The reads obtained from the sequencer are trimmed for quality using in-house–developed scripts. The trimmed reads are aligned to the reference genome using TopHat2. The transcript abundances and differences calculated using cuffdiff. The results were plotted using R and cummeRbund using in-house–developed scripts. Qlucore Omics Explorer version 3.2 (Qlucore AB) was used for identifying differentially expressed genes ($P < 0.05$) using a one-way ANOVA or a two-tailed Student's *t* test comparison. PCA plots, unsupervised hierarchical clustering, and heat maps were also generated in Qlucore. Ingenuity Pathway Analysis was used to carry out pathway analysis for differentially expressed genes across samples.

Flow Cytometry. For mitochondrial studies, BMDMs from WT and *Dhcr24*^{TG} mice were stained for 30 min with MitoSOX (2.5 μM, ThermoFisher, M36008) at 37 °C. Data were acquired with a BD FACSCalibur flow cytometer and analyzed with FloJo software (Tree Star, Inc). For the in vivo peritonitis model, peritonitis was induced by intraperitoneal injection with the NLRP3-specific inducer MSU (InvivoGen, No. tlrl-msu) crystals as described previously (36). Briefly, WT and *Dhcr24*^{TG} mice were injected with 1 mg MSU in PBS. After 6 h, the mice were euthanized, and total peritoneal cells were collected by lavage with 5 mL PBS with 1% FBS and 1 mM Hepes. Collected cells were counted by hemacytometer, and the proportion of $CD45^+$/$Ly6G^+$ neutrophils in the lavage was analyzed by flow cytometry using a BD LSR II systems. Absolute neutrophil numbers were calculated.

Seahorse Analysis of Mitochondrial Respiration. Isolated BMDMs were seeded at 100,000 cells per well on XF96 V3-PS cell culture microplates in complete media. Next day, the seeded cells were treated with 1 μg/mL LPS for 4 h in Dulbecco's modified Eagle's medium supplemented with 10% LPDS before subjected to two different assay media for measuring fatty acid oxidation (FAO) or glycolysis. Oxygen consumption rate (OCR) and extracellular acidification rate (ECAR) were examined using the XF96 Seahorse Metabolic Analyzer from Seahorse Biosciences. For FAO assay, media was supplemented with 100 μM BSA-Palmitate, 100 μM L-Carnitine, and 10 mM 2-Deoxy Glucose (to inhibit glycolysis). Mitochondrial bioenergetics was assessed in the absence or presence of 100 μM etomoxir through measurement of OCR changes in response to the following compounds: 1 μM oligomycin (portA), 2 μM FCCP (portB), and 2.5 μM rotenone/antimycin A mixture (portC). Measures of glycolysis and glycolytic capacity were determined by recording ECAR in response to sequential injections of 20mM glucose (portA), 2 μM Oligomycin (portB), and 10 mM 2-deoxyglucose (portC). OCR and ECAR data were then normalized to cell counts measured by fluorescence reading at 355-nm excitation and 460-nm emission following Hoechst staining (37). $n = 3$ to 5 mice per genotype, $n = 4$ to 15 replicates per mouse. Experiments were repeated a minimum of three times.

Mitochondria Isolation. BMDMs isolated from WT and *Dhcr24*^{TG} mice were seeded in 10-cm dishes (1×10^7/dish), and cell lysates were prepared using a Mitochondria Isolation Kit (Miltenyi Biotec, Cat No. 130-096-946) according to the manufacturer's instructions. Mitochondria were labeled and isolated with anti-TOM22 MicroBeads and snap frozen in liquid nitrogen for further lipidomics analysis. The lipid level in mitochondria was normalized based on total protein content using the DC protein assay). The purification of isolated mitochondria was analyzed with Western blot by Tomm20 (mitochondria marker) and Calnexin (ER marker) antibody.

Electron Microscopy and Mitochondrial Analysis. BMDMs were fixed with 2.5% glutaraldehyde and 2% PFA in 0.1 M sodium cacodylate (pH 7.4) for 2 h at RT. Cells were postfixed in 1% OsO_4 in the same buffer for 1 h, then stained en bloc with 2% aqueous uranyl acetate for 30 min, dehydrated in a graded series of ethanol to 100%, and embedded in Poly/bed 812 for 24 h. Thin sections (60 nm) were cut with a Leica ultramicrotome and poststained with uranyl acetate and lead citrate. Digital images were taken using a Morada charge-coupled device camera fitted with iTEM imaging software (Olympus). Mitochondria analysis was performed as described previously (38). A blinded investigator manually traced mitochondria profiles using ImageJ software. Mitochondria cross-sectional area and mitochondria aspect ratio (major axis divided by minor axis, minimum value is 1.0) were calculated as a measurement of mitochondria size and shape, respectively. Probability plots

were utilized to estimate changes in mitochondria size and shape, and statistical differences were tested using Kolmogorov–Smirnov test. Mitochondria density was estimated by dividing the number of mitochondria profiles by the cytosolic area. Mitochondria coverage was estimated by dividing the total area of mitochondria by the cytosolic area.

Aortic Singlet Preparation for Lipid Probe-Based Flow Cytometry. Single-cell suspensions of the aorta and BODIPY 493/503 staining were prepared as previously reported with minor modifications (15). Briefly, the aorta was carefully dissected, and perivascular fat was removed. Aortic tissue was cut into small pieces and subjected to enzymatic digestion with 1.5 mg/mL Collagenase A and 0.5 mg/mL Elastase (Worthington, Cat No. LS006365) for 40 min at 37 °C while shaking. The digested aortas were passed through a 70-μm cell strainer to obtain single-cell suspensions followed by incubation of 10 min at 4 °C with 10 μg/mL of purified rat anti-mouse FcgRII/III (Biolegend) to block nonspecific binding of antibodies to Fc receptors. Cells were subsequently stained with Live/Dead Fixable Blue Dead Cell Stain Kit (Invitrogen, Cat No. L23105), PE anti-mouse CD45.2 (Biolegend, Cat No. 109807), PE/Cyanine 7 anti-mouse CD64 [Biolegend] at 139313), and Pacific Blue anti-mouse/human CD11b (Biolegend, Cat No. 101223) followed by staining with 40 nM/L BODIPY 493/503 in PBS at 4 °C for 30 min. Viable $CD45^+CD11b^+$ $CD64^+$ cells were sorted by a FACS Aria III (BD Biosciences).

Mendelian Randomization of DHRC24 Expression and Atherosclerosis Diagnosis. To assess causal association between aortic expression of DHCR24 and atherosclerosis, we collected summary statistics from UK Biobank GWAS studies (http://www.nealelab.is/uk-biobank) and selected atherosclerosis-related traits (general atherosclerosis diagnosis -ICD10: I70-, peripheral atherosclerosis -DM_PERIPHATHERO-, or total circulating cholesterol -30690_irnt- or LDL -30780_irnt). Tissue-specific eQTL data for aortic artery were obtained from GTEX Version 8 (39). Slope and slope SE of SNPs with significant eQTLs for DHRC24 in "Artery aorta" were used as instrumental variable and beta and SE of beta for corresponding SNPs in the GWAS of interest were identified as outcome to calculate Mendelian randomization (the R package Mendelian Randomization found in ref. 40. In the MR model, we used linkage disequilibrium matrix data for all the SNPs calculated from LDLink (https://ldlink.nci.nih.gov:443/) to correct for SNPs that were not segregating independely. The model shown is derived from Inverse-variance weighted method, but all the other methods tested also showed significant correlations. Data cleaning, processing, and plotting was done with custom-made Python 3.6 scripts.

Statistical Analysis. All data are expressed as mean ± SEM. Statistical differences were measured using either unpaired two-sided Student's *t* test, one-way ANOVA (followed by the Dunnett's post hoc test) or two-way ANOVA (followed by the Bonferroni post hoc test). Normality was checked using the Kolmogorov–Smirnov test. A value of $P \leq 0.05$ was considered statistically significant. Data analysis was performed using GraphPad Prism Software Version 7.0 (GraphPad).

Data Availability. RNAseq and scRNA-seq data have been deposited in Gene Expression Omnibus (GSE175312 and GSE172374).

ACKNOWLEDGMENTS. We thank Nenad Sestan and members in his laboratory at Yale University for the analysis of the genomic data of this study. This work was supported at least in part by grants from the NIH (Grant Nos. R35HL135820 to C.F.-H., R35HL155988 to Y.S., and P01HL20948 to J.G.M.), the American Heart Association (Grant No. 20TPA35490416 to C.F.-H.), and the Academy of Finland (Grant Nos. 282192 and 312491 to E.I.). E.L.G. is funded by K99AG058801. J.O.-M. is a Howard Hughes Medical Institute Damon Runyon Cancer Research Foundation Fellow (DRG-2274-16).

1. C. K. Glass, J. L. Witztum, Atherosclerosis. The road ahead. *Cell* **104**, 503–516 (2001).
2. I. Tabas, G. García-Cardeña, G. K. Owens, Recent insights into the cellular biology of atherosclerosis. *J. Cell Biol.* **209**, 13–22 (2015).
3. K. J. Williams, I. Tabas, The response-to-retention hypothesis of early atherogenesis. *Arterioscler. Thromb. Vasc. Biol.* **15**, 551–561 (1995).
4. K. J. Moore, F. J. Sheedy, E. A. Fisher, Macrophages in atherosclerosis: A dynamic balance. *Nat. Rev. Immunol.* **13**, 709–721 (2013).
5. I. Tabas, K. E. Bornfeldt, Intracellular and intercellular aspects of macrophage immunometabolism in atherosclerosis. *Circ. Res.* **126**, 1209–1227 (2020).
6. J. van Tuijl, L. A. B. Joosten, M. G. Netea, S. Bekkering, N. P. Riksen, Immunometabolism orchestrates training of innate immunity in atherosclerosis. *Cardiovasc. Res.* **115**, 1416–1424 (2019).
7. E. Araldi *et al.*, Lanosterol modulates TLR4-mediated innate immune responses in macrophages. *Cell Rep.* **19**, 2743–2755 (2017).
8. E. V. Dang, J. G. Cyster, Loss of sterol metabolic homeostasis triggers inflammasomes - how and why. *Curr. Opin. Immunol.* **56**, 1–9 (2019).
9. E. V. Dang, J. G. McDonald, D. W. Russell, J. G. Cyster, Oxysterol restraint of cholesterol synthesis prevents AIM2 inflammasome activation. *Cell* **171**, 1057–1071.e11 (2017).
10. N. J. Spann *et al.*, Regulated accumulation of desmosterol integrates macrophage lipid metabolism and inflammatory responses. *Cell* **151**, 138–152 (2012).
11. S. L. Sabol, H. B. Brewer Jr., S. Santamarina-Fojo, The human ABCG1 gene: Identification of LXR response elements that modulate expression in macrophages and liver. *J. Lipid Res.* **46**, 2151–2167 (2005).
12. A. Venkateswaran *et al.*, Control of cellular cholesterol efflux by the nuclear oxysterol receptor LXR alpha. *Proc. Natl. Acad. Sci. U.S.A.* **97**, 12097–12102 (2000).
13. N. A-Gonzalez *et al.*, Apoptotic cells promote their own clearance and immune tolerance through activation of the nuclear receptor LXR. *Immunity* **31**, 245–258 (2009).
14. X. Rong *et al.*, LXRs regulate ER stress and inflammation through dynamic modulation of membrane phospholipid composition. *Cell Metab.* **18**, 685–697 (2013).
15. K. Kim *et al.*, Transcriptome analysis reveals nonfoamy rather than foamy plaque macrophages are proinflammatory in atherosclerotic murine models. *Circ. Res.* **123**, 1127–1142 (2018).
16. M. Pascual-García *et al.*, Reciprocal negative cross-talk between liver X receptors (LXRs) and STAT1: Effects on IFN-γ-induced inflammatory responses and LXR-dependent gene expression. *J. Immunol.* **190**, 6520–6532 (2013).
17. P. Duewell *et al.*, NLRP3 inflammasomes are required for atherogenesis and activated by cholesterol crystals. *Nature* **464**, 1357–1361 (2010).
18. E. L. Mills, B. Kelly, L. A. J. O'Neill, Mitochondria are the powerhouses of immunity. *Nat. Immunol.* **18**, 488–498 (2017).
19. T. Próchnicki, E. Latz, Inflammasomes on the crossroads of innate immune recognition and metabolic control. *Cell Metab.* **26**, 71–93 (2017).
20. J. J. Fuster *et al.*, Clonal hematopoiesis associated with TET2 deficiency accelerates atherosclerosis development in mice. *Science* **355**, 842–847 (2017).
21. G. Tumurkhuu *et al.*, Ogg1-dependent DNA repair regulates NLRP3 inflammasome and prevents atherosclerosis. *Circ. Res.* **119**, e76–e90 (2016).
22. M. Westerterp *et al.*, Cholesterol efflux pathways suppress inflammasome activation, NETosis, and atherogenesis. *Circulation* **138**, 898–912 (2018).
23. S. Burgess, C. N. Foley, V. Zuber, Inferring causal relationships between risk factors and outcomes from genome-wide association study data. *Annu. Rev. Genomics Hum. Genet.* **19**, 303–327 (2018).
24. E. A. Dennis *et al.*, A mouse macrophage lipidome. *J. Biol. Chem.* **285**, 39976–39985 (2010).
25. P. C. Norris, D. Reichart, D. S. Dumlao, C. K. Glass, E. A. Dennis, Specificity of eicosanoid production depends on the TLR-4-stimulated macrophage phenotype. *J. Leukoc. Biol.* **90**, 563–574 (2011).
26. J. P. Andersen *et al.*, Aster-B coordinates with Arf1 to regulate mitochondrial cholesterol transport. *Mol. Metab.* **42**, 101055 (2020).
27. J. Sandhu *et al.*, Aster proteins facilitate nonvesicular plasma membrane to ER cholesterol transport in mammalian cells. *Cell* **175**, 514–529.e20 (2018).
28. K. N. Maxwell, J. L. Breslow, Adenoviral-mediated expression of Pcsk9 in mice results in a low-density lipoprotein receptor knockout phenotype. *Proc. Natl. Acad. Sci. U.S.A.* **101**, 7100–7105 (2004).
29. L. Goedeke *et al.*, MicroRNA-148a regulates LDL receptor and ABCA1 expression to control circulating lipoprotein levels. *Nat. Med.* **21**, 1280–1289 (2015).
30. G. X. Zheng *et al.*, Massively parallel digital transcriptional profiling of single cells. *Nat. Commun.* **8**, 14049 (2017).
31. R. Satija, J. A. Farrell, D. Gennert, A. F. Schier, A. Regev, Spatial reconstruction of single-cell gene expression data. *Nat. Biotechnol.* **33**, 495–502 (2015).
32. N. V. Guevara, H. S. Kim, E. I. Antonova, L. Chan, The absence of p53 accelerates atherosclerosis by increasing cell proliferation in vivo. *Nat. Med.* **5**, 335–339 (1999).
33. M. A. Mitsche, J. G. McDonald, H. H. Hobbs, J. C. Cohen, Flux analysis of cholesterol biosynthesis in vivo reveals multiple tissue and cell-type specific pathways. *eLife* **4**, e07999 (2015).
34. E. G. Bligh, W. J. Dyer, A rapid method of total lipid extraction and purification. *Can. J. Biochem. Physiol.* **37**, 911–917 (1959).
35. J. G. McDonald, D. D. Smith, A. R. Stiles, D. W. Russell, A comprehensive method for extraction and quantitative analysis of sterols and secosteroids from human plasma. *J. Lipid Res.* **53**, 1399–1409 (2012).
36. H. Shi *et al.*, NLRP3 activation and mitosis are mutually exclusive events coordinated by NEK7, a new inflammasome component. *Nat. Immunol.* **17**, 250–258 (2016).
37. X. Yang *et al.*, Tri-iodo-l-thyronine promotes the maturation of human cardiomyocytes-derived from induced pluripotent stem cells. *J. Mol. Cell. Cardiol.* **72**, 296–304 (2014).
38. M. O. Dietrich, Z. W. Liu, T. L. Horvath, Mitochondrial dynamics controlled by mitofusins regulate Agrp neuronal activity and diet-induced obesity. *Cell* **155**, 188–199 (2013).
39. GTEX Version 8. https://storage.googleapis.com/gtex_analysis_v8/single_tissue_qtl_data/GTEx_Analysis_v8_eQTL.tar. Accessed 6 March 2021.
40. O. Yavorska, J. Staley, MendelianRandomization: Mendelian Randomization Package. R package version 0.5.1. https://cran.r-project.org/web/packages/MendelianRandomization/index.html. Accessed 9 March 2021.